Controlled Synthesis, Formation Mechanism, and Great Enhancement of Red Upconversion Luminescence of $NaYF_4$:Yb^{3+}, Er^{3+} Nanocrystals/Submicroplates at Low Doping Level

Junwei Zhao,[†,‡] Yajuan Sun,[†] Xianggui Kong,*[,†] Lijin Tian,[†,‡] Yu Wang,[†,‡,§] Langping Tu,[†,‡,§] Jialong Zhao,[†] and Hong Zhang*[,§]

Key Laboratory of Excited-State Processes, Changchun Institute of Optics, Fine Mechanics and Physics, Chinese Academy of Sciences, Changchun 130033, P. R. China, Graduate School of Chinese Academy of Sciences, Beijing 100039, P.R. China, and Van't Hoff Institute for Molecular Sciences, University of Amsterdam, Nieuwe Achtergracht 166, 1018 WV Amsterdam, The Netherlands

Received: June 24, 2008; Revised Manuscript Received: September 13, 2008

Strong red upconversion luminescence of rare-earth ions doped in nanocrystals is desirable for the biological/biomedical applications. In this paper, we describe the great enhancement of red upconversion emission ($^4F_{9/2} \rightarrow {}^4I_{15/2}$ transition of Er^{3+} ion) in $NaYF_4$:Yb^{3+}, Er^{3+} nanocrystals at low doping level, which is ascribed to the effectiveness of the multiphonon relaxation process due to the existence of citrate as a chelator and cross relaxation between Er^{3+} ions. The dissolution−recrystallization transformation, governing both the intrinsic crystalline phase (cubic and/or hexagonal phase) and the growth regime (thermodynamic vs kinetic), is responsible for the phase control of the $NaYF_4$ crystals. The possible formation mechanism of the $NaYF_4$ crystals and the role of trisodium citrate which acts as a chelating agent and shape modifier are discussed in detail. It is also found that the $\alpha \rightarrow \beta$ phase transition is favored by the high molar ratio of fluoride to lanthanide and high hydrothermal temperature as well as long hydrothermal time.

Introduction

In recent years, upconversion luminescence of rare-earth fluoride nanocrystals has drawn considerable interest,[1−9] due to its potential applications in sensitive bioprobes.[10−12] Compared with the conventional fluorophores (e.g., cy5), upconverting phosphors have many conceivable advantages as fluorescence labeling materials, such as low photobleaching,[13] carrying out easily *in vivo* imaging upon the NIR irradiation with noninvasive and deep penetration to the tissue or cell,[14] improved signal-to-noise ratio due to the absence of autofluorescence and reduction of light scattering,[15,16] and feasibility of multiple labeling with different emissions under the same excitation. Upconversion emission of rare-earth (RE)-doped nanocrystals has been observed in various crystal structure hosts.[17−25] Up to now, hexagonal phase $NaYF_4$ has been regarded as the most efficient upconversion host material.[1,2] Precise control of the size, shape, and phase allows manipulation of the properties of the nanocrystals as desired.[26] Rare-earth ions, especially trivalent erbium, are much more suitable for the conversion of infrared to visible light (upconversion) due to their favorable electronic energy level structures. The excited states ($^4I_{9/2}$ and $^4I_{11/2}$) of Er^{3+} ions with long lifetimes can easily be populated with CW NIR irradiation. Yb^{3+} ions, used as a sensitizer, are efficient in promoting the upconversion process due to the high absorption cross section of the $^2F_{7/2}$ level of Yb^{3+} ions than that of the $^4I_{11/2}$ excited state of Er^{3+} ions.[27,28]

Compared with other synthetic routes in nanocrystal preparation, the hydrothermal method has the following advantages: (1) Synthesis occurs at relatively low reaction temperature (in general <250 °C). (2) Size, structure, and morphology of the products are subject to hydrothermal conditions and easy to be modified. (3) The purity of product is high owing to recrystallization in hydrothermal solution. (4) The required equipment and process are simple. In order to obtain small and uniform particles, organic additives are often used, e.g., EDTA and citrate. Previously, we reported that the size of the particles synthesized with citrate is smaller than that synthesized with EDTA due to their different chelating constants and molecular structure. The difference between EDTA and citrate in chelating structure might lead to different product morphology because of the influence of the chelator on growth orientation in the phase transformation process.[29] We have also synthesized YVO_4:Er^{3+} nanocrystals using trisodium citrate as a chelator via hydrothermal reaction.[30] Recently, the β-$NaReF_4$ (Re = Lu, Y, and Yb) microstructures have been prepared using the hydrothermal method by Li et al.[31]

In this work, we performed a systematic research on the synthetic mechanism and found that the special dissolution−recrystallization transformation mechanism, governing both the intrinsic crystalline phase (cubic and/or hexagonal phase) and the growth regime (thermodynamic vs kinetic), is responsible for the phase control of the final products and the surface energy controlled by selective absorption of citrate resulted in anisotropic morphology evolution of the $NaYF_4$ crystals. It is also found that high molar ratio of fluoride to lanthanide, high hydrothermal temperature, or long hydrothermal time is favorable to the $\alpha \rightarrow \beta$ phase transformation. In addition, the process of multiphonon relaxation (MR), when citrate is used as a chelator, is proven to play a role in the great enhancement of the red upconversion emission of Er^{3+} at low doping level, i.e., Yb^{3+} 10 mol %, Er^{3+} 1 mol % in both α- and β-$NaYF_4$ nanocrystals. Such an enhancement was usually observed at

* To whom correspondence should be addressed. Phone: +86-431-86176313(X.K.); +31-20-5256976(H.Z.). E-mail: xgkong14@ciomp.ac.cn (X.K.); h.zhang@uva.nl (H.Z.).

† Changchun Institute of Optics, Fine Mechanics and Physics, Chinese Academy of Sciences.

‡ Graduate School of Chinese Academy of Sciences.

§ University of Amsterdam.

10.1021/jp805567k CCC: $40.75
Published on Web 11/14/2008

TABLE 1: Synthesis Conditions and Characteristics of the Samples Prepared via the Hydrothermal Method

sample no.	NaF/citrate/Ln molar ratio	hydrothermal temperature (°C)	hydrothermal time (h)	phase	morphology	reference
1	4/0.5/1	200	2	α	sphere	Figure 1A
2	8/0.5/1	200	2	α	sphere	Figure 1B
3	12/0.5/1	200	2	*β*	plates	Figure 1C
4	12/0/1	180	2	α and *β*	rod and sphere	Figure 2A
5	12/0.5/1	180	2	α and *β*	plates and sphere	Figure 2B
6	12/1/1	180	2	α	sphere	Figure 2C
7	12/1.5/1	180	2	α	sphere	Figure 2D
8	12/0.5/1	160	2	α	sphere	Figure 3A
9	12/1.5/1	180	0	α	sphere	Figure 4A
10	12/1.5/1	180	1	α	sphere	Figure 4B
11	12/1.5/1	180	3	α	sphere	Figure 4D
12	12/1.5/1	180	4	α and *β*	grain	not shown

higher doping level and ascribed to cross relaxation (CR) when other chelators were used.

Experimental Section

1. Materials. All reagents were analytical grade. $Ln(NO_3)_3 \cdot 6H_2O$ (Ln = Y, Yb, and Er) salt was freshly prepared by the reaction of Ln_2O_3 with nitric acid. Water was distilled and deionized using a Millipore Milli-Q Purification System, which has a resistivity not less than 18.2 MΩ. Trisodium citrate was purchased from Beijing Chemical Plant (Beijing, China).

2. Synthesis of $NaYF_4$:Yb^{3+}, Er^{3+} Phosphors. In a typical procedure for the preparation of $NaYF_4$: 10 mol % Yb^{3+}, 1 mol % Er^{3+} nanoparticles, an aqueous solution of $Ln(NO_3)_3 \cdot 6H_2O$ (0.1 mol/L, lanthanide ion molar ratio, Y/Yb/Er = 89:10:1) was mixed with an aqueous solution of trisodium citrate under vigorous stirring, and a white precipitate of lanthanide citrate was formed. An aqueous solution of NaF was then added slowly into the above mixture, and the pH value was kept at ~6.5. After being stirred for 1 h, the resulting precursor solution was transferred to a 60 mL autoclave. The autoclave was then placed in a digital type temperature controlled oven and heated at the elevated temperature for several hours, and then allowed to cool down to room temperature naturally. Subsequently, the precipitate of $NaYF_4$:Yb^{3+}, Er^{3+} phosphors in the autoclave could be separated from the reaction media by centrifugation (6500 rpm, 15 min) and then washed several times with deionized water. After being dried in a vacuum at 60 °C for 24 h, $NaYF_4$:Yb^{3+}, Er^{3+} phosphor was obtained. Finally, the two picked representative samples were heated to 300 °C and were kept at the same temperature for 2 h under the protection of an argon atmosphere. Samples with other dopant parameters were prepared in a similar way.

3. Characterization. The structure and morphology of $NaYF_4$:Yb^{3+}, Er^{3+} phosphor were characterized by X-ray powder diffractometer (XRD), scanning electron microscopy (SEM), Fourier transform infrared (FT-IR) spectra, and transmission electron microscopy (TEM). The obtained samples were characterized by XRD using a Brucker D8-advance X-ray diffractometer with Cu Kα radiation (λ = 1.5418 Å); the operation voltage and current were 40 kV and 40 mA, respectively. The 2θ angle ranges from 15 to 60° with a step of 0.021 and counting time of 0.2 s. The size and morphology of $NaYF_4$:Yb^{3+}, Er^{3+} were characterized by field emission scanning electron microscopy (FESEM, Hitachi, S-4800). FT-IR spectra were recorded at a Perkin-Elmer 580B infrared spectrophotometer with the KBr pellet technique. In making the KBr pelletes, 1 mg of sample was diluted with approximately 100 mg of KBr power. The FT-IR spectra were collected in the spectral range 400−4000 cm^{-1}. Low- and high-resolution transmission electron microscopy (HRTEM) was performed applying an FEI Tecnai G2 S-Twin instrument with a field emission gun operating camera. The upconversion emission spectra of $NaYF_4$:Yb^{3+}, Er^{3+} phosphors were acquired using a Jobin-Yvon LabRam Raman spectrometer system equipped with 1800 and 600 grooves/mm holographic gratings, respectively, and a Peltier air-cooled CCD detector. The samples were excited by a CW semiconductor diode laser at 980 nm. The maximal excitation power used in the experiment was about 760 mW with a focusing area of about 0.03 mm^2. The upconversion luminescence spectra were measured under identical conditions in order to compare their relative emission intensities.

Results and Discussion

The synthetic conditions and characteristics of samples prepared via the hydrothermal route are listed in Table 1, where the optimal synthetic parameters for small, uniform nanoparticles are given, i.e., a molar ratio of NaF/citrate/Ln of approximately 12:1.5:1 and a hydrothermal time of 2−3 h at a temperature of 180 °C. For pure hexagonal $NaYF_4$ submicroplates, the optimal parameters include the following: molar ratio of NaF/citrate/Ln of approximately 12:0.5:1, hydrothermal time of 2−3 h at 200 °C. The pH values were kept at around 6−7 in all cases in order to explore the influence of other parameters. It turns out that the NaF/Ln molar ratio, citrate/Ln molar ratio, hydrothermal temperature, and hydrothermal time are the key factors for the crystal structure, size, and/or morphology of the nanocrystals.

1. Effect of NaF Content. To investigate the effect of the NaF content on the morphology, size, and structure of the as-prepared $NaYF_4$ nanocrystals, the NaF/Ln ratio was taken as 4, 8, and 12, respectively. The SEM images and XRD patterns of the nanocrystals are given in Figure 1. It can be seen that the as-prepared $NaYF_4$ nanocrystals are spherical with coarse surfaces when the NaF/Ln ratio is 4 (Figure 1A), indicating low crystallization of the sample.[29] When the ratio reaches 8, crystallization of the $NaYF_4$ nanoparticles is improved, as evidenced by the more regular shape and smoother surface (Figure 1B). When the ratio increases further to 12, however, pure hexagonal-shaped NaYF4 submicroplates are formed with the size of ~600 nm × 300 nm (side length × thickness, Figure 1C).

Furthermore, NaF content affects not only the shape and size but also the crystal structure of the samples. Figure 1D shows the corresponding XRD patterns of the $NaYF_4$ nanocrystals prepared with different NaF/Ln ratios. The bottom and middle XRD patterns depicted in Figure 1D (a and b) match very well with the standard face-centered cubic structure data (JCPDS card no. 77-2042), whereas the top XRD pattern shown in Figure 1D (c) coincides with the hexagonal phase $NaYF_4$ (JCPDS card no.16-0334). Note that the as-prepared sample without the

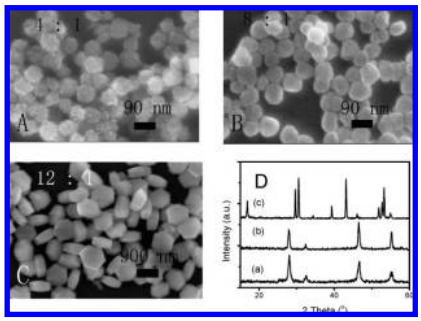

Figure 1. SEM images (A, B, and C) and XRD patterns (D) of $NaYF_4$:Yb^{3+}, Er^{3+} nanocrystals and submicroplates synthesized under different NaF/Ln ratios: (A and a) 4:1; (B and b) 8:1; (C and c) 12:1 (temperature = 200 °C. time = 2 h. citrate/Ln = 0.5).

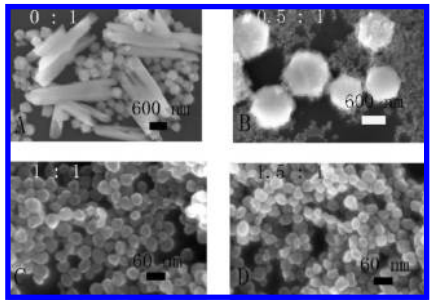

Figure 2. SEM images of $NaYF_4$:Yb^{3+}, Er^{3+} nanocrystals prepared under different citrate/Ln ratios: (A) 0:1; (B) 0.5:1; (C) 1:1; (D) 1.5:1 (temperature = 180 °C. time = 2 h. NaF/Ln = 12).

hydrothermal process is the cubic phase. The crystal structure must undergo transformation from the cubic phase to the hexagonal phase during hydrothermal treatment when the NaF/Ln ratio is equal to 12. Recently, Wang et al.[9] and Ghosh et al.[32] reported that, when the F^- ions are excessive, the β-$NaYF_4$ nanocubes and nanocrystals can be formed. In the synthesis of the $NaLnF_4$ crystals, F^- anions serve as a reactant as well as a mineralizer and the presence of an excess of F^- ions lowers remarkably the crystallization temparature.[33−35] Therefore, the amount of F^- ions affects significantly the crystallization of the product. Keeping hydrothermal conditions the same, the presence of excessive F^- favors the growth of the hexagonal $NaYF_4$ crystals. In order to investigate the influence of other parameters, the NaF/Ln ratio is kept at 12 unless specifically mentioned otherwise in the following text.

2. Effect of the Ratio of Citrate/Ln. It is known that the chelating agent is key to the size of particles and the aggregation; therefore, it can be used to prepare nanoparticles with small size and good dispersion.[7,29,30] To clearly demonstrate the effect of the citrate content on the $NaYF_4$ nanocrystals, the ratio of citrate/Ln was taken as 0, 0.5, 1, and 1.5, respectively. As shown in Figure 2, the obtained $NaYF_4$:Yb^{3+}, Er^{3+} nanocrystals exhibit different morphologies including spherical nanoparticles, nanorods, and submicroplates. The samples are composed of nanorods and spherical nanoparticles that aggregated together without citrate (see Figure 2A). Increasing the amount of citrate to a ratio of citrate/Ln of 0.5, a mixture of cubic nanoparticles and hexagonal submicroplates is obtained (Figure 2B). However, when the ratio reaches 1.0 and 1.5, pure nanoparticles with a size distribution of 30−50 nm are formed (Figure 2C and D), implying that the crystal growth is restricted. The corresponding XRD patterns demonstrate that cubic crystal structure is formed with the citrate/Ln ratio more than unity and the mixed crystal structures of cubic and hexagonal phases coexisted with the citrate/Ln ratio less than unity (see Supporting Information Figure S1). Recently, Li et al. showed that the presence of citrate can restrict the growth of the β-$NaYF_4$ hexagonal microprism.[31b] These results indicate that citrate can be used to control the size and the morphology of the particles as well as the crystal phase. Because of the strong coordination effect of the carboxylate and hydroxyl group of the citrate with lanthanide ions in the aqueous solution, the $\alpha \rightarrow \beta$ phase transformation is hindered. Relevant discussion is going to be detailed in the following sections.

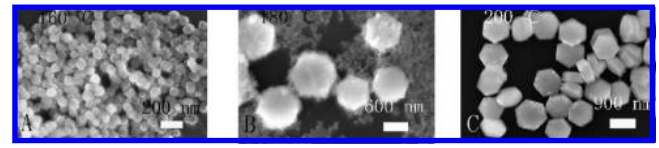

Figure 3. SEM images of $NaYF_4$:Yb^{3+}, Er^{3+} nanocrystals prepared under different temperatures: (A) 160 °C; (B) 180 °C; (C) 200 °C (time = 2 h. citrate/Ln = 0.5. NaF/Ln = 12).

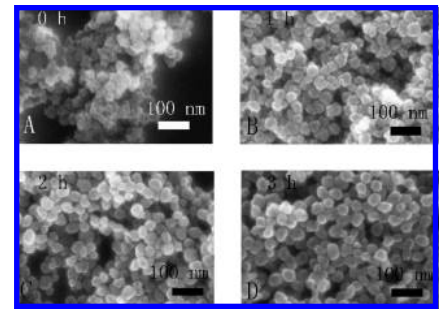

Figure 4. SEM images of $NaYF_4$:Yb^{3+}, Er^{3+} nanocrystals prepared with different hydrothermal times: (A) 0 h; (B) 1 h; (C) 2 h; (D) 3 h (temperature = 180 °C. citrate/Ln = 1.5. NaF/Ln = 12).

3. Effect of the Hydrothermal Temperature. The effect of the hydrothermal temperature on the size and morphology of nanocrystals was also examined. Increasing the hydrothermal temperature from 160 to 200 °C leads to completely different morphology and size of the products (Figure 3). Lower hydrothermal temperature favors the formation of smaller size nanoparticles, whereas higher hydrothermal temperature benefits the formation of mix-shaped nanocrystals or submicroplates. The corresponding XRD patterns verify that the nanoparticles are in the cubic phase while the submicroplates are in the hexagonal phase (see Supporting Information Figure S2). Therefore, it can be concluded that high hydrothermal temperature can provide energy that is required for the transformation from α- to β-phase $NaYF_4$ and the activation of specific faces for the anisotropic growth of pure β-$NaYF_4$ nanocrystals.

4. Effect of the Hydrothermal Time. It is expected that the hydrothermal time influences the size, shape, and crystallization of the nanophosphors. The hydrothermal time was set from 0 to 3 h at 180 °C with a citrate/Ln ratio of 1.5. From the SEM images shown in Figure 4, it is clear that the sample without hydrothermal treatment appeared as aggregates of many primary particles with a coarse surface (Figure 4A). When the hydrothermal time extends from 1 to 3 h, the size of the nanoparticles increases slightly due to the presence of citrate which restricted the growth of the nanoparticles and their surface becomes smooth. The corresponding XRD patterns are shown in Supporting Information Figure S3. All of the diffraction peaks match closely with the α-$NaYF_4$ structure with the hydrothermal time less than 3 h. The intensity of diffraction peaks becomes sharper and stronger with the extension of the hydrothermal time due to the improved crystallization and the increased size of the as-prepared samples. When the hydrothermal time is longer than 3 h, some diffraction peaks characteristic of

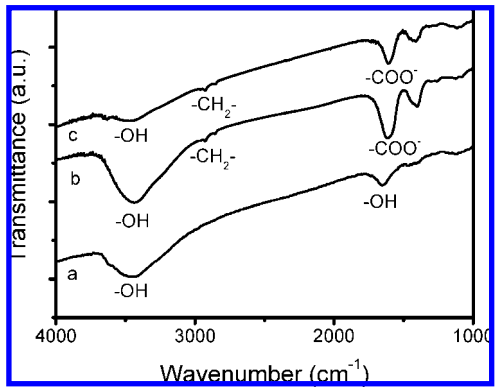

Figure 5. FT-IR spectra of the $NaYF_4$:Yb^{3+}, Er^{3+} phosphors: (a) mixed shape, without citrate; (b) nanoparticles, citrate/Ln = 1.5; (c) submicrocrystals, citrate/Ln = 0.5.

β-$NaYF_4$ appear in the XRD pattern (not shown). It should be mentioned that with lower citrate/Ln ratio (e.g., 0.5) the $\alpha \rightarrow \beta$ phase transformation occurs in a shorter hydrothermal time (e.g., 2 h). Recently, it was reported that pure β-$NaYF_4$ and β-$NaYbF_4$ microplates can be obtained at 180 °C for 2 and 2.5 h with a citrate/Ln ratio equal to 1, respectively.[31b,c] These primary results indicate that the long hydrothermal time facilitates the crystallization and growth of nanocrystals. As mentioned above, the formation of the hexagonal phase needs higher thermal energy than that of the cubic phase. It seems that long hydrothermal time is beneficial for the transformation from α- to β-phase $NaYF_4$:Yb^{3+}, Er^{3+}, by supplying energy to speed up the dissolution, renucleation, and crystallization process.

5. Formation Mechanism of α-$NaYF_4$ Nanocrystals and β-$NaYF_4$ Submicrocrystals under Hydrothermal Conditions. As discussed above, the nanocrystals are spherical particles in the cubic phase before hydrothermal treatment. After hydrothermal treatment, the samples undergo changes in crystallization, size, shape, and crystal structure. High NaF/Ln ratio and high hydrothermal temperature and/or long hydrothermal time favor the formation of β-$NaYF_4$ crystals. The presence of excess F^- ions decreases remarkably the crystallization temperature,[33−35] which indicates that the hexagonal $NaYF_4$ can be obtained in the presence of excessive F^- ions at lower temperature. It is supported that the hexagonal phase is a thermodynamically stable phase and more ordered and the transition from the cubic to hexagonal phase [$Fm3m \rightarrow P63/m$] is a disorder-to-order change.[1,32]

Here, one might have a question: what is the original driving force for the structure transformation and morphology evolution in solution under mild hydrothermal conditions? To this end, we recall that a two-stage model is well accepted to exist in the formation of the $NaYF_4$ phosphors: nucleation and crystal growth. The controlled release of Ln cations from the Ln−citrate complex helps to separate the nucleation and growth stages. Furthermore, the decomplexed citrate anions would attach to the surface of the nanocrystals and lead to formation of well-dispersible nanocrystals in water. FT-IR spectra can be instructive at this point. Figure 5 shows the FT-IR spectra of the representative $NaYF_4$:Yb^{3+}, Er^{3+} phosphors. In Figure 5a, the absorption bands around 3400 and 1650 cm^{-1} of the sample without citrate correspond to the OH stretching and deformation vibrations,[36] respectively, which arise from the absorption of H_2O. The absorption band around 3400 cm^{-1} in Figure 5b and c may be the vibration superposition of the hydroxyl groups of the water and citrate absorbed at the surface of the $NaYF_4$:Yb^{3+}, Er^{3+} nanocrystals/submicroplates. The weak bands at about 2927 and 2850 cm^{-1} are assigned to the asymmetrical and symmetrical stretching vibration modes, respectively, of the CH_2 group.[37] The peaks at about 1610 and 1400 cm^{-1} are assigned to vibrations of the carboxylate anion in the citrate,[36,38] which proves the presence of the citrate ligands at the surface of the nanoparticles/submicroplates. The influence of nucleation rate on the particle size has been discussed in detail in our previous study.[29] In the crystal growth stage, a delicate balance between the thermodynamic growth and kinetic growth regimes can strongly control the final structure of the nanocrystals.[39,40] When the thermodynamic growth regime is driven by a sufficient supply of thermal energy (*KT*), the most stable crystal structure is preferred. Crystallographic phase transformation in solution usually undergoes a dissolution−recrystallization process in order to minimize the surface energy of the system.[41] Mai et al. have reported that the energy barrier is the main reason for α-$NaReF_4$ formation.[42] It is reported also that the phase transition from α-$NaYF_4$ to β-$NaYF_4$ is mainly due to the modification of the environment of Y^{3+} occupation sites, including coordination number.[43] Y^{3+} or other cationic sites are conveniently coordinated by F^- ions with increasing fluoride concentration (12:1), which would decrease the energy barrier, and as a result, an ordered hexagonal structure appears. Otherwise, a less ordered cubic structure should be obtained at low NaF/Ln ratio (4:1). This result supports the conclusion that fluoride concentration plays an important role in tuning the crystal structure.[9,32] Furthermore, it is confirmed that low hydrothermal temperature and short hydrothermal time are not beneficial for the transformation from α- to β-$NaYF_4$, mainly because of the lack of enough energy to overcome the energy barrier and to speed up the dissolution, renucleation, and crystallization process.

The thermodynamic behavior of small particles is different from that of the bulk material by the free energy term γA, the product of the surface (or interface) free energy and the surface (or interfacial) area.[44−46] When the different surface area of polymorphs of the same materials possesses different free energies in the growth stage, the change in phase stability can occur in response to both the changes in surface environment and particle size. In our case, tuning the citrate/Ln ratio of the growth solution is a crucial step in the control of the size and morphology of $NaYF_4$. There are a number of roles that the added citrate may play in the synthesis. The major one is to modulate the thermodynamics and kinetics of nucleation and growth of the system by controlling the interfacial tension (surface free energy). According to the chelating properties of citrate, increasing the citrate amount decreases the interfacial free energies of the system.[47] In this work, we speculate that, during the growth of $NaYF_4$ nanocrystals, the chelator (citrate) might selectively bind to the certain crystal surface of the nanocrystals, which results in the surface free energies of the various crystallographic planes differing significantly and renders the anisotropic growth along crystallographically reactive directions, as reported previously for the formation of β-$NaReF_4$ hexagonal microplates.[31] Figure 6 shows the representative TEM and HRTEM images of the β-$NaYF_4$ hexagonal submicroplates parallel to the substrate. The very regular hexagonal cross section can be clearly observed (Figure 6A). In the corresponding HRTEM image, taken with the electron beam perpendicular to the edge of the submicroplates, the interplanar distance between adjacent lattice fringes is determined as about 0.53 nm (Figure 6B), which corresponds to the *d*-spacing value of the $(10\bar{1}0)$ planes.[31] The selected area electron diffraction (SEAD) patterns are consistent with a hexagonal phase structure of $NaYF_4$ (Figure 6B, inset), demonstrating its

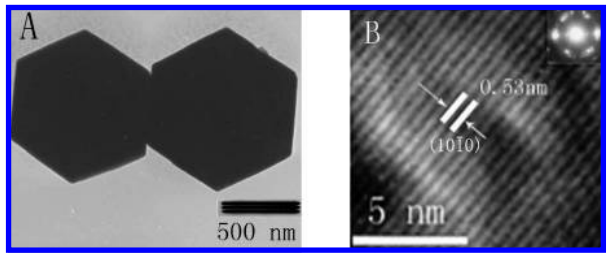

Figure 6. (A) TEM and (B) HRTEM images of β-$NaYF_4$ submicroplates lying flate on the substrate. Inset: The SEAD patterns of β-$NaYF_4$ submicroplates.

single-crystalline nature. According to our observation, when a small amount of citrate is used (e.g., the citrate/Ln ratio is less than unity) under the same hydrothermal conditions, the phase transformation from α- to β-$NaYF_4$ occurs easily at low hydrothermal temperature and/or short hydrothermal time. In this way, thermodynamic colloidal instability could be expected; i.e., in the specific reaction circumstance (hydrothermal treatment), the primarily thermodynamic stable state (α-$NaYF_4$) becomes thermodynamic unstable, resulting in a considerable promoting of the ripening processes. The particles of α-$NaYF_4$ spontaneously grow by an Ostwald-ripening process to reach a new thermodynamic equilibrium state, where the β-$NaYF_4$ structure is more thermodynamically stable than the α-$NaYF_4$ phase, henceforth, making the phase transformation occur. During the growth stage, citrate might specifically bind to the {0001} facets of β-$NaYF_4$ nuclei, which lowers the surface energy of these facets, where typical growth in the [0001] direction is prohibited, and the growth of nuclei is driven along six symmetric directions: $\pm[10\bar{1}0]$, $\pm[1\bar{1}00]$, and $\pm[01\bar{1}0]$, which directly resulted in the formation of β-$NaYF_4$ submicroplates. When the citrate/Ln ratio is more than unity, the interfacial free energies of the system are further depressed and there are enough citrate molecules which can bind to every crystal surface of α-$NaYF_4$ nuclei. As a result, the surface energy of every growth direction is reasonably the same and the structure transformation from the cubic to hexagonal phase is thus hindered. The thermodynamic equilibrium state is conserved during the growth stage of the nanocrystals. Obviously, the crystal structure of $NaYF_4$ nanocrystals can be controlled by tuning the citrate/Ln ratio of the growth solution.

In summary, there are two kinds of key factors that determine the final shapes of α-$NaYF_4$ nanoparticles and β-$NaYF_4$ submicroplates. The first one is the dissolution−recrystallization transformation, which is responsible for the α → β phase transformation. The anisotropic structure of the thermodynamically stable β-$NaYF_4$ seeds induces the anisotropic growth along their crystallographically reactive directions. The second one is the citrate anions used as the chelating agents and shape modifiers, which play an important role in restraining the structure transformation from the cubic to hexagonal phase and inducing the formation of the β-$NaYF_4$ submicroplates.

6. Upconversion Luminescence Spectroscopy of $NaYF_4$: Yb^{3+}, Er^{3+} Phosphors. Figure 7 shows the upconversion luminescence spectra of the α-$NaYF_4$: 10 mol % Yb^{3+}, 1 mol % Er^{3+} nanoparticles prepared at 180 °C for 0, 1, 2, and 3 h with a citrate/Ln ratio of 1.5 upon irradiation of 980 nm wavelength. The green emission in the 510−570 nm region is assigned to the ($^2H_{11/2}$, $^4S_{3/2}$) → $^4I_{15/2}$ transition, and the red emission in the 620−690 nm region is assigned to the $^4F_{9/2}$ → $^4I_{15/2}$ transition of the Er^{3+} ion in the $NaYF_4$ nanocrystalline.[6,7,12] To investigate the upconversion luminescence mechanism, the pump power dependence of luminescence intensity was per-

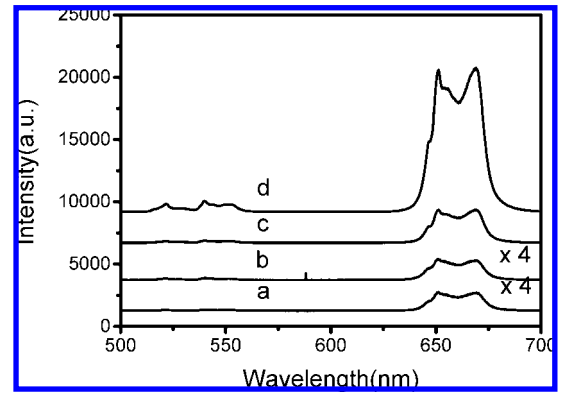

Figure 7. The upconverted fluorescence spectra of $NaYF_4$: 10 mol % Yb^{3+}, 1 mol % Er^{3+} nanoparticles prepared under different hydrothermal times upon radiation of 980 nm wavelength (power = 550 mW): (a) 0 h; (b) 1 h; (c) 2 h; (d) 3 h (temperature = 180 °C. citrate/Ln = 1.5. NaF/Ln = 12).

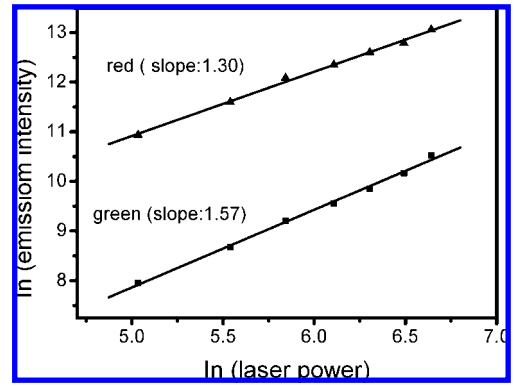

Figure 8. Pump power dependence of the upconverted green and red integrated intensities of $NaYF_4$: 10 mol % Yb^{3+}, 1 mol % Er^{3+} nanocrystals under 980 nm excitation.

formed. It is well-known that $I_{em} \propto I_P^n$ exists in upconversion processes, where n denotes the number of NIR photons absorbed to generate one frequency upconverted photon. The pump power dependence is exemplified in Figure 8. Fitting the data points yielded approximately slopes of 1.57 and 1.30 for the ($^2H_{11/2}$, $^4S_{3/2}$) → $^4I_{15/2}$ and $^4F_{9/2}$ → $^4I_{15/2}$ transitions, respectively, indicating that the upconversion luminescence involves a two-photon absorption process. The slopes are deviated from 2, which could be ascribed to the competition between different decay channels within the intermediate state, including MR to the lower-lying state, radiatively decay to the ground state, upconversion from the intermediate state, and nonradiative trapping.[48] Inefficient nonradiative channels favor the upconversion process, i.e., higher n. In our case, the MR process should be efficient due to the presence of citrate (*vide infra*). In a Yb^{3+} and Er^{3+} codoped system, two main upconversion mechanisms are usually taken into account: (i) energy transfer (ET) from Yb^{3+} to Er^{3+} ions and (ii) a CR process between two nearby Er^{3+} ions (Figure 9).

As can be seen from Figure 7, the upconversion luminescence intensity of the sample without hydrothermal treatment is the lowest. The upconversion luminescence intensities of the samples under hydrothermal treatment for 0 and 1 h are magnified 4 times for the sake of comparison. The upconversion luminescence intensity increases remarkably with the particle size increasing. Besides, the intensities of the red emission are much stronger than that of the green one. It should be mentioned that a similar phenomenon is also observed in β-$NaYF_4$: 10 mol % Yb^{3+}, 1 mol % Er^{3+} submicroplates (Figure 10). To

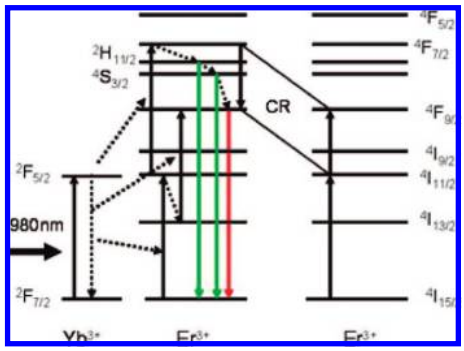

Figure 9. A schematic illustration of the upconversion luminescence processes of $NaYF_4$:Yb^{3+}, Er^{3+} crystals.

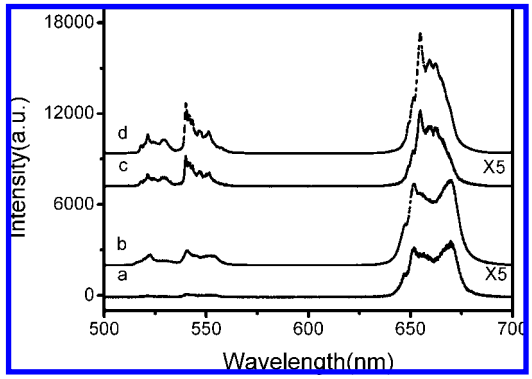

Figure 10. Upconverted fluorescence spectra of the α-$NaYF_4$: 10 mol % Yb^{3+}, 1 mol % Er^{3+} nanoparticles and the β-$NaYF_4$: 10 mol % Yb^{3+}, 1 mol % Er^{3+} submicroplates before (solid) and after (dashed) annealing at 300 °C for 2 h: (a) cubic, before annealing; (b) cubic, after annealing; (c) hexagonal, before annealing; (d) hexagonal, after annealing (power = 550 mW).

disentangle this question, the population mechanism of the $^4F_{9/2}$ level should be clarified. The energy level $^4F_{9/2}$ for the red emission ($^4F_{9/2} \rightarrow {}^4I_{15/2}$) can be populated via the following processes: the first one is direct population from the $^4I_{13/2}$ level, which can be populated through the nonradiative relaxation of the $^4I_{11/2}$ level, the second one is via a nonradiative relaxation from the $^4S_{3/2}$ level, and the third one is by a CR process of $^4F_{7/2} \rightarrow {}^4F_{9/2}$ and $^4I_{11/2} \rightarrow {}^4F_{9/2}$ between the two nearby Er^{3+} ions. The two former processes emphasize the importance of multiphonon relaxation. In our case, the MR process is regarded as an efficient process due to the presence of the organic groups on the surface of the nanoparticles (see IR spectra in Figure 5). The hydroxyl group possesses high-energy vibrational modes (2700−3600 cm^{-1}), compared with the dominant phonon modes in $NaYF_4$ which lie between 300 and 400 cm^{-1}.[3] These high-energy vibrations would strongly quench the excited states of Er^{3+} ions by multiphonon relaxation and thus impact the upconversion processes significantly. The MR rate, W_p, can be expressed as follows:[49]

$$W_p = A \exp(-Bp) \quad (1)$$

$$p \approx \Delta E/\hbar\omega \quad (2)$$

where A (in hertz) and B are constants, p is phonon numbers needed in the multiphonon relaxation, ΔE is the energy gap to the next lower level, and $\hbar\omega$ is the phonon energy. For the Er^{3+} ions, the $^4I_{11/2}$ and $^4I_{13/2}$ states are the intermediate levels responsible for green and red emissions, respectively. There is an energy gap of ~3600 cm^{-1} between the $^4I_{11/2}$ and $^4I_{13/2}$ states and ~3000 cm^{-1} between the $^4S_{3/2}$ and $^4F_{9/2}$ states. According to eq 1, the high-energy vibrations from hydroxyl groups make the MR ($^4I_{11/2} \rightarrow {}^4I_{13/2}$ and $^4S_{3/2} \rightarrow {}^4F_{9/2}$) much more probable than that of the intrinsic phonons in the $NaYF_4$ host, where at least seven phonons are required to bridge these gaps. As is well-known, the upconversion intensity depends on the population of the intermediate states. Therefore, the presence of the hydroxyl group on the surface would result in an enhanced red emission and reduced green emission if they are coupled with Er^{3+} ions.

To validate this point, the two representative samples were annealed at 300 °C for 2 h. The SEM images and the XRD patterns indicate that the size, shape, and crystal structure are unchanged (see Supporting Information Figures S4 and S5). The upconversion luminescence spectra of the α-$NaYF_4$:Yb^{3+} 10 mol %, Er^{3+} 1 mol % nanoparticles and the β-$NaYF_4$:Yb^{3+} 10 mol %, Er^{3+} 1 mol % submicroplates before and after annealing are shown in Figure 10. The upconversion luminescence intensity of the unannealing samples is magnified 5 times for the sake of comparison. The upconversion luminescence intensity is enhanced greatly after annealing treatment due to the reduction of the quenching centers.[27] Notably, the red-to-green (R/G) ratio decreases from 22.1 to 7.0 for the α-$NaYF_4$:Yb^{3+} 10 mol %, Er^{3+} 1 mol % nanoparticles, while the R/G ratio changes from 3.07 to 2.91 for the β-$NaYF_4$:Yb^{3+} 10 mol %, Er^{3+} 1 mol % submicroplates. This indicates that the MR is much more efficient in α-$NaYF_4$:Yb^{3+} 10 mol %, Er^{3+} 1 mol % nanoparticles than in the β-$NaYF_4$:Yb^{3+} 10 mol %, Er^{3+} 1 mol % submicroplates owing to the larger surface-to-volume ratio. The larger the surface-to-volume ratio is, the more Er^{3+} ions are located at/near the surface of the nanoparticles relative to the Er^{3+} ions in the core. Er^{3+} ions located in the surface layer coupled strongly with the high vibrational modes of the organic groups and thus experience more efficient nonradiative relaxation from higher electronic levels to lower electronic levels, leading to the unusual enhancement of the red upconversion emission. Moreover, different chelators, which have different chelating structure, vibrational modes, and coupling capability, will produce the different crystallization of the product because of their influences on the nucleation and growth processes.[29] A citrate molecule has four binding sites, including three carboxyl groups and one hydroxyl group, among which three sites can be bound with Ln^{3+} ions.[29] In our case, the ligands of citrate molecules might couple strongly with Er^{3+} ions, which lead to high R/G ratio of upconversion emission of the $NaYF_4$: Yb^{3+}, Er^{3+} crystals.

To testify the influence of the CR process on the upconversion emission at different sensitizer concentrations, the spectra of the samples doped with 1 mol % Er^{3+} and 0, 1, 2, 5, and 10 mol % Yb^{3+} ions were investigated. The R/G ratio as a function of Yb^{3+} concentration is shown in Figure 11. The R/G ratio changes with the concentration of the Yb^{3+} ions. As the Yb^{3+} ion concentration increases from 0 to 10 mol %, the R/G ratios are about 1.7, 3.1, 9.6, 14.9, and 22.1, correspondingly. At high Yb^{3+} ion concentration, green emission is almost entirely restrained. Due to the higher absorption cross section of the $^2F_{7/2}$ level of Yb^{3+} ions than that of the $^4I_{11/2}$ state of Er^{3+} ions when pumping at 980 nm and the fact that the two energy levels are more or less even, the energy from the efficient excitation of Yb^{3+} can be transferred effectively to Er^{3+} ions. With the increase of Yb^{3+} concentration, the ET process becomes more efficient and induced more population in the $^4I_{11/2}$ or $^4F_{7/2}$ levels of the Er^{3+} ions. Thereby, the strong resonant CR of the type $^4F_{7/2} \rightarrow {}^4F_{9/2}$ and $^4I_{11/2} \rightarrow {}^4F_{9/2}$ between two nearby Er^{3+} ions occurs, resulting in more population of the $^4F_{9/2}$ state and a strong red emission. This is another reason for high R/G ratio of

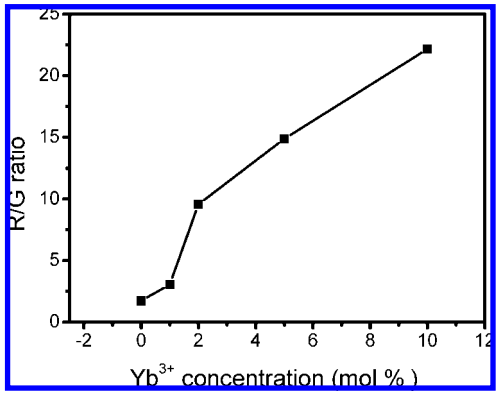

Figure 11. R/G of upconversion luminescence as a function of Yb^{3+} concentration in α-$NaYF_4$:Yb^{3+}, Er^{3+} nanoparticles under radiation of 980 nm wavelength (power = 550 mW).

upconversion emission of the samples. Similar phenomena were also observed in Y_2O_3: Yb^{3+}, Er^{3+} nanocrystals.[50] However, when other chelators were used to prepare $NaYF_4$: Yb^{3+}, Er^{3+} nanocrystals, the abnormal strong red upconversion emission is not observed even at Yb^{3+} 10 mol % and Er^{3+} 2 mol % doping concentration.[29] Therefore, in our case, we speculate that the MR process is the main reason for high R/G ratio of the $NaYF_4$: Yb^{3+}, Er^{3+} crystals.

Conclusions

The Yb^{3+} and Er^{3+}codoped α-$NaYF_4$ nanoparticles and *β*-$NaYF_4$ hexagonal-shaped submicroplates are successfully prepared by a hydrothermal reaction using the citrate−yttrium−nitrate complex as the precursor. An unusual red upconversion enhancement at low doping concentration is observed, which is ascribed to the abnormal strong phonon assistant nonradiative relaxation, in relation with the usage of citrate as a chelator, and CR between Er^{3+} ions. Besides, the synthetic mechanism is systematically studied in detail and optimal reaction parameters are given. The results of this study are important for the application of the nanoparticles as a platform in biology and biomedicine.

Acknowledgment. This work was financially supported by NSFC of China, Nation "863", and the exchange program between CAS of China and KNAW of The Netherlands. The first author is also grateful to Dr. Xin Wang (Suzhou Institute of Nanotech and Nanobionics, CAS) for helpful discussions.

Supporting Information Available: XRD patterns of $NaYF_4$: Yb^{3+}, Er^{3+} nanocrystals/submicroplates prepared under different citrate/Ln ratios (S1), at different hydrothermal temperatures (S2), and under different hydrothermal times (S3); SEM images (S4) and XRD patterns (S5) of the $NaYF_4$:Yb^{3+}, Er^{3+} nanoparticles/submicroplates before and after annealing at 300 °C for 2 h. This material is available free of charge via the Internet at http://pubs.acs.org.

References and Notes

(1) Krämer, K. W.; Biner, D.; Frei, G.; Güdel, H. U.; Hehlen, M. P.; Lüthi, S. R. *Chem. Mater.* **2004**, *16*, 1244.
(2) Menyuk, N.; Dwight, K.; Pierce, J. W. *Appl. Phys. Lett.* **1972**, *21*, 159.
(3) Suyver, J. F.; Grimm, J.; van Veen, M. K.; Biner, D.; Krämer, K. W.; Güdel, H. U. *J. Lumin.* **2006**, *117*, 1.
(4) Yi, G. S.; Chow, G. M. *Adv. Funct. Mater.* **2006**, *16*, 2324.
(5) Heer, S.; Kömpe, K.; Güdel, H. U.; Haase, M. *Adv. Mater.* **2004**, *16*, 2102.
(6) Zeng, J. H.; Su, J.; Li, Z. H.; Yan, R. X.; Li, Y. D. *Adv. Mater.* **2005**, *17*, 2119.
(7) Yi, G. S.; Lu, H. C.; Zhao, S. Y.; Ge, Y.; Yang, W. J.; Chen, D. P.; Guo, L. H. *Nano Lett.* **2004**, *4*, 2191.
(8) Schäfer, H.; Ptacek, P.; Kömpe, K.; Haase, M. *Chem. Mater.* **2007**, *19*, 1396.
(9) Wang, L. Y; Li, Y. D. *Chem. Mater.* **2007**, *19*, 727.
(10) van de Rijke, F.; Zijlmans, H.; Li, S.; Vail, T.; Raap, A. K.; Niedbala, R. S.; Tanke, H. J. *Nat. Biotechnol.* **2001**, *19*, 273.
(11) Lim, S. F.; Riehn, R.; Ryu, W. S.; Khanarian, N.; Tung, C. K.; Tank, D.; Austin, R. H. *Nano Lett.* **2006**, *6*, 169.
(12) Wang, L. Y.; Li, Y. D. *Chem. Commun.* **2006**, *24*, 2557.
(13) Chan, W. C. W.; Nie, S. M. *Science* **1998**, *281*, 2016.
(14) Chatterjee, D. K.; Rufaihah, A. J.; Zhang, Y. *Biomaterials* **2008**, *29*, 937.
(15) Zijlmans, H. J. M. A.; Bonnet, J.; Burton, J.; Kardos, K.; Vail, T.; Niedbala, R. S.; Tanke, H. J. *Anal. Biochem.* **1999**, *267*, 30.
(16) Feijo, J. A.; Moreno, N. *Protoplasma* **2004**, *223*, 1.
(17) Patra, A.; Friend, C. S.; Kapoor, R.; Prasad, P. N. *J. Phys. Chem. B* **2002**, *106*, 1909.
(18) Patra, A.; Friend, C. S.; Kapoor, R.; Prasad, P. N. *Chem. Mater.* **2003**, *15*, 3650.
(19) Vetrone, F.; Christopher Boyer, J.; Capobianco, J. A.; Speghini, A.; Bettinelli, M. *J. Phys. Chem. B* **2003**, *107*, 1107.
(20) Stouwdam, J. W.; van Veggel, F. C. J. M. *Nano Lett.* **2002**, *2*, 733.
(21) Vetrone, F.; Christopher Boyer, J.; Capobianco, J. A.; Speghini, A.; Bettinelli, M. *Chem. Mater.* **2003**, *15*, 2737.
(22) Vetrone, F.; Christopher Boyer, J.; Capobianco, J. A. *J. Phys. Chem. B* **2002**, *106*, 5622.
(23) Capobianco, J. A.; Vetrone, F.; Boyer, J. C.; Speghini, A.; Bettinelli, M. *Opt. Mater.* **2002**, *19*, 259.
(24) Zhang, H. X.; Kam, C. H.; Zhou, Y.; Han, X. Q.; Buddhudu, S.; Lam, Y. L. *Opt. Mater.* **2000**, *15*, 47.
(25) Wang, X.; Kong, X. G.; Shan, G. Y.; Yu, Y.; Sun, Y. J.; Feng, L. Y.; Chao, K. F.; Lu, S. Z.; Li, Y. J. *J. Phys. Chem. B* **2004**, *108*, 18408.
(26) Ghosh, P.; Oliva, J.; Rosa, E. D. L.; Haldar, K. K.; Solis, D.; Patra, A. *J. Phys. Chem. C* **2008**, *112*, 9650.
(27) StrohhÖfer, C.; Polman, A. *J. Appl. Phys.* **2001**, *90*, 4314.
(28) Oliveira, A. S.; raujo de, M. T.; Gouveia-Neto, A. S. *Appl. Phys. Lett.* **1998**, *72*, 753.
(29) Sun, Y. J.; Chen, Y.; Tian, L. J.; Yu, Y.; Kong, X. G.; Zhao, J. W.; Zhang, H. *Nanotechnology* **2007**, *18*, 275609.
(30) Sun, Y. J.; Liu, H. J.; Wang, X.; Kong, X. G.; Zhang, H. *Chem. Mater.* **2006**, *18*, 2726.
(31) (a) Li, C. X.; Yang, J.; Yang, P. P.; Zhang, X. M.; Lian, H. Z.; Lin, J. *Cryst. Growth Des.* **2008**, *8*, 923. (b) Li, C. X.; Quan, Z. W.; Yang, J.; Yang, P. P.; Lin, J. *Inorg. Chem.* **2007**, *46*, 6329. (c) Li, C. X.; Quan, Z. W.; Yang, P. P.; Yang, J.; Lian, H. Z.; Lin, J. *J. Mater. Chem.* **2008**, *18*, 1353.
(32) Ghosh, P.; Patra, A. *J. Phys. Chem. C* **2008**, *112*, 3223.
(33) Estermann, M.; Mclusker, L. B.; Baerlocher, C; Merrouche, A.; Kessler, H. *Nature* **1991**, *352*, 320.
(34) Bukovec, P.; Bukuvel, N.; Demsar, A. *J. Therm. Anal.* **1990**, *36*, 1751.
(35) Zhao, C. Y.; Feng, S. H.; Chao, Z. C.; Shi, C. S.; Xu, R. R.; Ni, J. Z. *Chem. Commun.* **1996**, *14*, 1641.
(36) Lin-Vien, D.; et al. *The Handbook of IR and Raman Characteristic Frequencies of Organic Molecules*; Academic Press: New York, 1991; p 137.
(37) Socrates, G. *Infrared Characteristic Group Frequencies*; Wiley: New York, 1980.
(38) Wang, Y.; Wong, J. F.; Teng, X. W.; Lin, X. Z.; Yang, H. *Nano Lett.* **2003**, *3*, 1555.
(39) Jun, Y. W.; Jung, Y. Y.; Cheon, J. *J. Am. Chem. Soc.* **2002**, *124*, 615.
(40) Jun, Y. W.; Choi, J. S.; Cheon, J. *Angew. Chem., Int. Ed.* **2006**, *45*, 3414.
(41) Vayssieres, L.; Beermann, N.; Lindquist, S. E.; Hagfeldt, A. *Chem. Mater.* **2001**, *13*, 233.
(42) Mai, X. H.; Zhang, W. Y.; Si, R.; Yan, G. Z.; Sun, D. L.; You, P.; Li Yan, H. C. *J. Am. Chem. Soc.* **2006**, *128*, 6426.
(43) Mathews, D. M.; Ambekar, R. B.; Tyagi, K. A.; Köhler, J. *J. Alloys Compd.* **2004**, *377*, 162.
(44) McHale, J. M.; Aurous, A.; Perotta, A. J.; Navrotsky, A. *Science* **1997**, *277*, 788.
(45) Zhang, H. Z.; Banfield, J. F. *J. Mater. Chem.* **1998**, *8*, 2073.
(46) Zhang, H. Z.; Gilbert, B.; Huang, F.; Banfield, J. F. *Nature* **2003**, *424*, 1025.
(47) Tian, Z. R.; Voigt, J. A.; Liu, J.; Mckenzie, B.; Mcdermott, M. J.; Rodriguez, M. A.; Konishi, H.; Xu, H. F. *Nat. Mater.* **2003**, *2*, 821.
(48) Pollnau, M.; Gamelin, D. R.; S. R. Lüthi, S. R.; Güdel, H. U. *Phys. Rev. B* **2000**, *61*, 3337.
(49) Schmidt, T.; Müller, G.; Spanhel, L. *Chem. Mater.* **1998**, *10*, 65.
(50) Vetrone, F.; Christopher Boyer, J.; Capobianco, J. A. *J. Appl. Phys.* **2004**, *96*, 661.

JP805567K